

arXiv:1409.5048v1 [physics.flu-dyn] 17 Sep 2014

arXiv:1409.5048v1 [physics.flu-dyn] 17 Sep 2014

- arXiv:1409.5048v1 [physics.flu-dyn] 17 Sep 2014

arXiv:1409.5048v1 [physics.flu-dyn] 17 Sep 2014

arXiv:1409.5048v1 [physics.flu-dyn] 17 Sep 2014

arXiv:1409.5048v1 [physics.flu-dyn] 17 Sep 2014

arXiv:1409.5048v1 [physics.flu-dyn] 17 Sep 2014

arXiv:1409.5048v1 [physics.flu-dyn] 17 Sep 2014

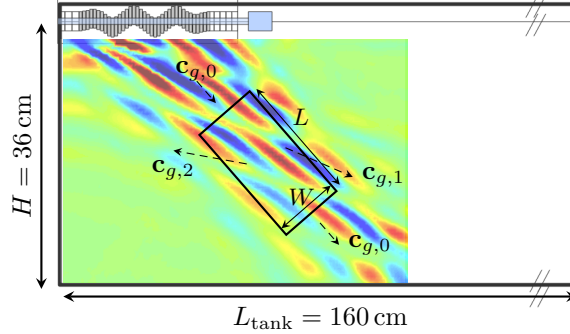


Figure 1: Sketch of the set-up. Experimentally, the wave generator is lying horizontally at the top of the wave tank. The vertical density gradient field of a typical wave beam generated at the top of the domain and undergoing PSI is presented as background of the figure. The dashed arrows indicate the group velocity of the three wave beams. The tilted rectangle of length L and width W corresponds to the control area used in the model.

2. Experimental and numerical approach

2.1. Experimental set-up.

A tank 160 cm large, 17 cm wide is filled with 36 cm of linearly stratified salt water with constant buoyancy frequency N . An internal wave of wavelength λ_0 is generated using a wave generator (Gostiaux et al. 2007; Mercier et al. 2010) placed horizontally with a plane wave configuration identical to the one used by Bourget et al. (2013). Note that to avoid spurious emission of internal waves on the extremities of the moving region, the amplitude of the plates is constant over n wavelengths in the central region, while one half-wavelength with a smooth decrease of the amplitude is added on each side. The beam width $W = (n + 1)\lambda_0$ is varied from λ_0 to $5\lambda_0$ by changing the horizontal extent of the moving part of the wavemaker. A schematic view of the experimental set-up is shown in figure 1. Synthetic Schlieren technique (Dalziel et al. 2000; Sutherland et al. 1999) is used to obtain the two-dimensional instantaneous density gradient field ($\bar{\rho}_x(x, z, t) = \partial_x(\rho(x, z, t) - \rho_0(z))$, $\bar{\rho}_z(x, z, t) = \partial_z(\rho(x, z, t) - \rho_0(z))$) where $\rho(x, z, t)$ and $\rho_0(z)$ are the instantaneous and initial fluid densities. Series of experiments are performed varying the horizontal wave number ℓ_0 , the plate motion amplitude a and the frequency ω_0 . It results in variations of the vertical wave number m_0 according to the dispersion relation $\omega_0/N = \ell_0/\kappa_0$, as well as variations of Ψ_0 , the amplitude of the stream function ψ , which is defined such that $\partial_z\psi = -u$ and $\partial_x\psi = v$ with u and v the horizontal and vertical components of the velocity. The parameters used in this article are summarized in Table 1. A typical experimental result is presented as background of figure 1.

2.2. Numerical method

In addition to the experiments, we performed 2D direct numerical simulations with the finite elements commercial software Comsol Multiphysics. The simulations solve the incompressible continuity equation, the Navier-Stokes equation for a Newtonian fluid in the Boussinesq approximation and the equation of salinity conservation. All elements are triangular standard Lagrange mesh of type $P_2 - P_3$ (i.e. quadratic for the pressure field but cubic for the velocity and density fields). The total number of degree of free-

Configuration	N (rad s ⁻¹)	ω_0/N	ℓ_0 (m ⁻¹)	Ψ_0/ν	W	Approach
I	0.89	0.85	110	16.9	1 - 5 λ_0	Experimental
II	0.89	0.85	110	16.9	2 - 3 λ_0	Numerical
III	0.91	0.74	75	33	3 λ_0	Experimental
IV	0.91	0.74	75	33	3 λ_0	Numerical
V	0.91	0.74	75	33	20 λ_0	Numerical

Table 1: Experimental and numerical parameters, with N the buoyancy frequency, ω_0 the frequency of the primary wave, ℓ_0 the horizontal wave number, $\Psi_0 = v_0/\ell_0$ the experimentally measured amplitude of the stream function in which v_0 is the vertical velocity, ν the viscosity and W the width of the primary beam.

dom is larger than 2 millions. At each time step, the system is solved with the Backward Difference Formulae (BDF) temporal solver and the sparse direct linear solver PAR-DISO. The Comsol BDF solver automatically adapts its scheme order between 1 and 5 (see details in Hindmarsh et al. (2005): it varies between 1 and 3 during our calculations. Note that no stabilization technique has been used. The Schmidt number, which compares diffusivity of salt and momentum is set to $Sc = 10$ as a proxy for the value $Sc = 700$ existing in the laboratory configuration. To prevent the creation of a reflected beam at the bottom of the domain, an attenuation layer is added wherein viscosity and diffusivity of salt increase exponentially with depth. To mimic the wavemaker of the experimental set-up, the horizontal velocity, the vertical velocity and the density are simultaneously imposed at each time-step at the top horizontal boundary and correspond to linear gravity waves. The amplitude of the imposed velocities and density is constant over n wavelengths in the central region, while one half-wavelength with a smooth decrease of the amplitude is added on each side similar to the experimental configuration. On the left and the bottom of the domain, we impose no stress and no flux and on the right, the pressure anomaly is fixed to zero, with no viscous stress and flux. Note that at time $t = 0$, the linear viscous beam is imposed in the bulk. The advantage of the numerical approach is that the beam width can be varied to much larger value than five wavelengths.

2.3. Results.

Let us first focus on the experimental and numerical results of configurations I and II. Figures 2(a) and 2(c) present the time evolution of the vertical density gradients measured at a given point in the experiment (configuration I), while figures 2(b) and 2(d) show the same information for the numerical simulation (configuration II). Experimental and numerical results display a good agreement, evidencing the following observation : while for a beam width $W = 2\lambda_0$ (figures 2(a,b)), the regular signal does not show any triadic resonance, in the case where $W = 3\lambda_0$ (figures 2(c,d)), the instability develops, as emphasized by the modulation of the signal, typical of the apparition of new frequencies in the system. Moreover, frequencies and wavelengths of the secondary waves present a good agreement, as can be seen in Table 2. For experiments with $W = 4\lambda_0$ and $5\lambda_0$ (not shown), the instability is observed as well. Experimental and numerical results thus reveal for the first time the critical role of the beam width in the occurrence of the triadic instability.

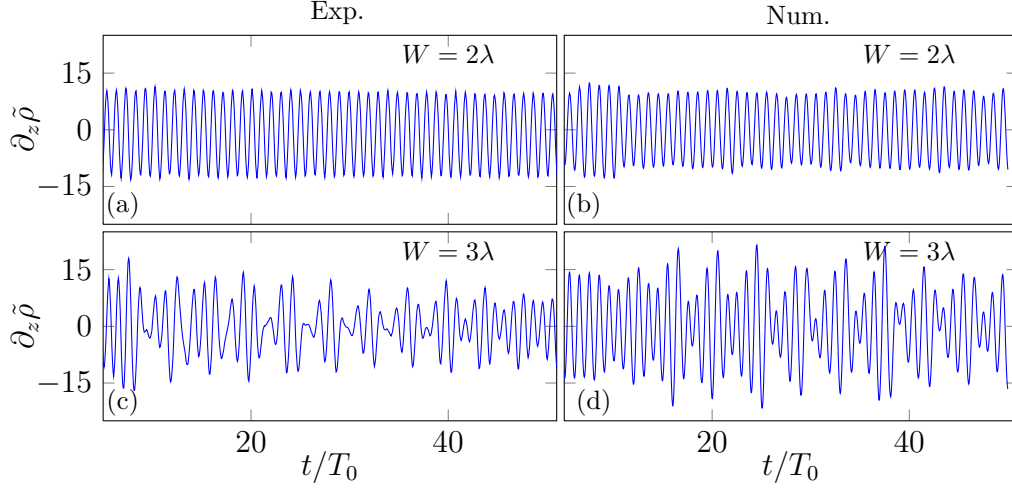


Figure 2: Time evolution of the amplitude of $\partial_z \tilde{\rho}$ [kg.m^{-4}] 4.5 cm below the wave maker and in the middle of the beam as the width of the beam is increased from $W = 2\lambda_0$ (upper panels) to $3\lambda_0$ (lower panels) for configurations I-II ($\omega_0/N = 0.85$, $\ell_0 = 110 \text{ m}^{-1}$, $\psi_0/\nu = 16.9$). Experimental results are shown in left panels and numerical ones in right panels.

Configuration	W (rad s^{-1})	ω_1/N	κ_1 (m^{-1})	ω_2/N	κ_2 (m^{-1})	Approach
I	$3 - 5 \lambda_0$	0.64	220	0.25	120	Experimental
II	$3 \lambda_0$	0.60	201	0.26	101	Numerical
III	$3 \lambda_0$	0.49	208	0.26	121	Experimental
IV	$3 \lambda_0$	0.49	232	0.25	148	Numerical
V	$20 \lambda_0$	0.50	147	0.27	61	Numerical

Table 2: Experimental and numerical values of ω_1 and ω_2 , the frequencies of the secondary waves and κ_1 and κ_2 , the wave vector modulus of the secondary waves.

3. Theory

To understand this observation, it is crucial to realize that the theory of PSI is derived for infinitely extended plane waves, as described in Koudella & Staquet (2006) and Bourget et al. (2013). We thus propose to take into account the *width* of the primary wave beam, the guiding idea being that the two secondary plane waves can exit the spatial extent of the primary wave beam (McEwan & Plumb 1977; Gerkema et al. 2006). Once they have left this region, they cannot interact any more with the primary plane wave and the energy transfer is broken.

To perform an energy balance, let us define a control area within the primary wave beam as presented by the tilted rectangle in figure 1. For simplicity, we neglect the spatial attenuation of the waves in this area, i.e. the surface energy densities E_0 , E_1 and E_2 of the different waves are considered uniform. Consequently, the temporal variation of the primary plane wave energy in the domain is due to:

- i) nonlinear interactions that transfer energy from the primary wave to both secondary ones (denoted $\Gamma_{\text{int}}(i, j)$ where i and j represent the two other waves of the triad);
- ii) viscosity;
- iii) incoming and outgoing flux of the primary wave.

For the domain $W \times L$, this can be summarized as

$$\frac{dE_0}{dt} LW = \Gamma_{\text{int}}(1, 2) - \nu \kappa_0^2 E_0 LW + E_{\text{in}} W c_{g,0} - E_0 W c_{g,0}, \quad (3.1)$$

with E_{in} the surface energy injected by the generator and $c_{g,0} = (N^2 - \omega_0^2)^{1/2} / \kappa_0$.

Assuming that PSI occurs everywhere in the beam, the outgoing energy flux of the secondary waves through the cross beam faces with width W is compensated by the incoming one. In contrast, since they do not propagate parallel to the primary beam, they exit the control area also from the lateral boundaries without compensation. For the temporal variation of the secondary waves energy in the domain, this leads to

$$\frac{dE_i}{dt} LW = \Gamma_{\text{int}}(0, j) - \nu \kappa_i^2 E_i LW - E_i L |\mathbf{c}_{g,i} \cdot \mathbf{e}_{k_0}|, \quad (3.2)$$

with $i = 1, 2, j = 2, 1$ and the modulus of the group velocity $c_{g,i} = (N^2 - \omega_i^2)^{1/2} / \kappa_i$.

The first term represents the interaction with the other plane waves of the triadic resonance while the third one accounts for the energy exiting the control area. As $E_i \propto \kappa_i^2 \Psi_i \Psi_i^*$, using the infinite width expression (Bourget et al. 2013) for the interaction terms, one gets

$$\frac{d\Psi_0}{dt} = -|I_0| \Psi_1 \Psi_2 - \frac{\nu}{2} \kappa_0^2 \Psi_0 + F, \quad (3.3)$$

$$\frac{d\Psi_1}{dt} = +|I_1| \Psi_0 \Psi_2^* - \left(\frac{\nu}{2} \kappa_1^2 + \frac{|\mathbf{c}_{g,1} \cdot \mathbf{e}_{k_0}|}{2W} \right) \Psi_1, \quad (3.4)$$

$$\frac{d\Psi_2}{dt} = +|I_2| \Psi_0 \Psi_1^* - \left(\frac{\nu}{2} \kappa_2^2 + \frac{|\mathbf{c}_{g,2} \cdot \mathbf{e}_{k_0}|}{2W} \right) \Psi_2, \quad (3.5)$$

with I_i the interaction term defined as follows

$$I_i = \frac{\ell_j m_r - m_j \ell_r}{2\omega_i \kappa_i^2} \left[\omega_i (\kappa_j^2 - \kappa_r^2) + \ell_i N^2 \left(\frac{\ell_j}{\omega_j} - \frac{\ell_r}{\omega_r} \right) \right] \quad (3.6)$$

with $i, j, r = 0, 1, 2$ and $F = c_{g,0} (\Psi_{\text{in}}^* \Psi_{\text{in}} - \Psi_0^* \Psi_0) / (2L \Psi_0^*)$ a forcing term, corresponding to the difference between the incoming energy and the outgoing one for the primary wave.

The solution for Ψ_1 and Ψ_2 can be easily obtained with the hypothesis Ψ_0 constant. One finds exponentially growing solutions with growth rate

$$\sigma_{\pm} = -\frac{1}{4} (\Sigma_1 + \Sigma_2) \pm \sqrt{\frac{1}{16} (\Sigma_1 - \Sigma_2)^2 + |I_1| |I_2| |\Psi_0|^2}, \quad (3.7)$$

where $\Sigma_i = \nu \kappa_i^2 + \sigma_{\text{adv}}(\kappa_i)$ and $\sigma_{\text{adv}}(\kappa_i) = |\mathbf{c}_{g,i} \cdot \mathbf{e}_{k_0}| / W$, the inverse of an advection time since it characterizes the transport of the secondary waves energy out of the interaction region. The viscous part of the expression of Σ_i is similar to the expression obtained in McEwan & Plumb (1977) in the limit of large Prandtl number.

Cases with large σ_{adv} values will present a very strong finite-width effect. Three parameters impact the value of the growth rate:

(a) The width W of the beam. The term σ_{adv} varies like the inverse of W , thus the growth rate is decreased when the beam is narrow. On the contrary, when W goes to infinity, σ_{adv} vanishes and the growth rate of the original theory (Bourget *et al.* 2013) is recovered.

(b) The amplitude of the group velocities of the secondary waves. When the modulus of the secondary wave vector κ_i is small, the group velocity increases and the secondary waves exit the primary wave beam more rapidly. So there is less time for them to grow in amplitude. Besides, σ_{adv} is weaker for low stratification N (small group velocity) at κ and ω fixed, which implies a stronger instability in the oceans where N is weak compared with laboratory conditions.

(c) The direction of the group velocity of each waves of the triad. When the secondary waves are almost perpendicular to the primary plane wave, they leave the interaction area quickly, which does not favor the instability. To summarize, this finite-width effect is stronger when the group velocity of the secondary wave is aligned with \mathbf{k}_0 .

For configurations I and II presented in figure 2, the above model predicts that the growth rate is an increasing function of W . For an infinitely wide wave beam, the instability occurs for any value of the amplitude (see appendix). In contrast, for finite width beams, a non vanishing threshold appears. For example, for $W = 2\lambda_0$, the maximum growth rate becomes negative for $\Psi_0/\nu < 4.4$. Moreover, during the finite duration of the experiment, even if the instability occurs, the amplitude of the two secondary waves might be too small to be detected. For example, we can define a detection criterion by requiring that for the secondary waves to be detected, the duration of the experiment must exceed 3 times the inverse of the growth rate. With this criterion, in the case of an infinitely wide wave beam, the instability can only be observed during the experiment if $\Psi_0/\nu > 1.6$ whereas for $W = 2\lambda_0$, the threshold is five times higher, $\Psi_0/\nu > 8.5$. Interestingly, this value of amplitude threshold has the same order of magnitude as the imposed amplitude in configurations I and II, notwithstanding the simplifying hypothesis made by neglecting spatial attenuation in the longitudinal (viscous decay) and transversal (imposed wave beam shape) direction of the primary wave. Therefore, the above model gives an explanation why the instability occurs in these two configurations only for W larger than $3\lambda_0$.

This new analysis reveals a dramatic effect on the development of the triad instability which has been totally overlooked before. When the beam gets narrower, the PSI cut-off, initially due only to viscosity, is displaced towards a larger forcing amplitude so that at a given amplitude, the instability can be completely suppressed by decreasing the beam width.

4. Selection of the triad.

We will now show that the finite-width effect can also result in a specific triad selection. To do that, we focus on the results for another set of parameters (Configurations III-V, see Table 1), this case is therefore different from the previous one. Experimental and numerical wave fields (respectively configurations III and IV) presented in figures 3(a) and 3(b) are in good agreement. As underlined by Bourget *et al.* (2013), the theoretical prediction for an infinite primary plane wave is that for this set of parameters (configurations III-IV), the wavelength of one of the secondary waves generated by the instability is larger than the primary wavelength, while the other one is smaller (see Table 2). In this case, the energetic transfer will occur towards larger and smaller scales simultaneously. However, this prediction was not verified and a different type of triad was observed experimentally in Bourget *et al.* (2013), with transfer to smaller

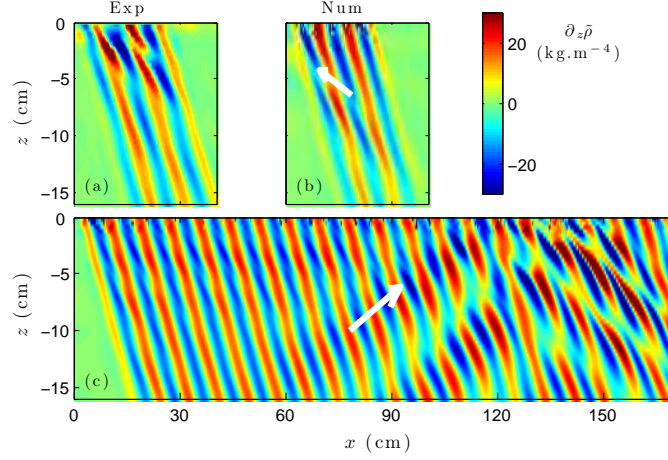


Figure 3: Vertical density gradient fields for configurations III-V ($\omega_0/N = 0.74$, $\ell_0 = 75 \text{ m}^{-1}$, $\psi_0/\nu = 33$). a) Experiments with $W = 3\lambda_0$; b) simulations with $W = 3\lambda_0$; c) simulations with $W = 20\lambda_0$. The two vectors represent the direction of the group velocity for one of the two secondary plane waves.

scales only. This difference between the prediction and the observations can again be traced back to the finite width of the wave beam. To demonstrate that, we rely on numerical results since the experimental set-up cannot generate plane waves with a beam size larger than $6\lambda_0$. Note that we have performed numerical simulations for $6\lambda_0$ (yielding similar results as for $3\lambda_0$), and $10\lambda_0$ (yielding similar results as for $20\lambda_0$). Therefore, we do not show these results here and focus only on the extreme cases $3\lambda_0$ and $20\lambda_0$. Figure 3(c) shows the results of configuration V, i.e. for the same parameters but for a significantly wider beam ($20\lambda_0$). The primary wave beam is still unstable, but the secondary waves look quite different compared to the results for $W = 3\lambda_0$. To quantify the differences, a temporal Hilbert transform (Mercier et al. 2008) and a spatial Fourier transform are used to measure the different wave vectors present in the numerical density gradient fields. These vectors are shown in figures 4(a) and 4(b). In addition, the curves in these figures represent the location of the tip of all possible wave vectors \mathbf{k}_1 satisfying the theoretical resonance conditions with a growth rate possessing a positive real part. A clear difference between the two cases is visible. For $W = 3\lambda_0$, a single triad is observed and its secondary wave vectors \mathbf{k}_1 belongs to an external branch of the theoretical resonance loci ($\ell_1 > \ell_0$). The wavelengths of both secondary waves are smaller than the primary wavelength. For $W = 20\lambda_0$, two different triads are measured. The first one (dashed vectors), with secondary vector $\mathbf{k}_{1,e}$ lying on an external branch (hence the subscript “e”), is similar to the one found for smaller W . For the second one (solid vectors), its secondary vector $\mathbf{k}_{1,c}$ is located in the central region of the theoretical loci curve ($0 < \ell_1 < \ell_0$). In this case, one secondary wave has a larger wavelength than the primary wave and the other a smaller one.

These observations can be explained by the finite-width theoretical approach presented previously: the predicted evolution of the maximum value of the growth rate as a function of W is shown in figure 4(c). The growth rates were computed separately for the external (\circ symbols) and central ($+$ symbols) cases. A transition between the two possible triads is predicted around $W_c = 7\lambda_0$. For $W < W_c$, the most unstable triad is on the external branch. The corresponding predicted location of the tip of wave

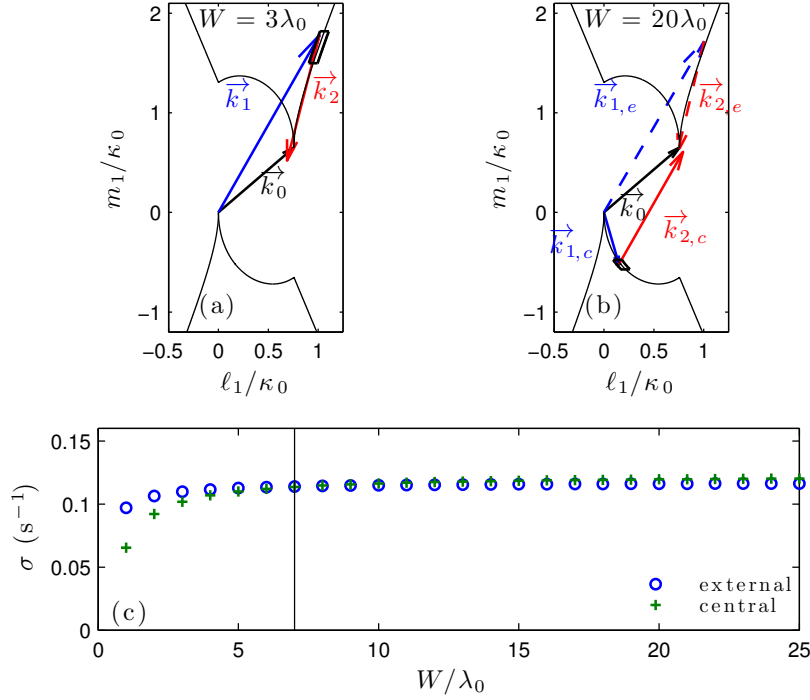


Figure 4: (color online) a) The three arrows are the measurements of the three wave vectors for the numerical case $W = 3\lambda_0$. b) The five arrows are the measurements of the wave vectors for the numerical case $W = 20\lambda_0$. In a) and b), the dark solid line represents the theoretical resonance loci for the secondary wave vector \vec{k}_1 for a given \vec{k}_0 and the rectangles represent the most unstable mode for the present finite-width model. c) Evolution of the growth rate computed from (3.7) as a function of the width of the beam, computed using the finite-size model. The transition between the external and central triad configurations is obtained around $W = 7\lambda_0$ (vertical line).

vector \vec{k}_1 is displayed as a rectangle in figure 4(a), showing a very good agreement with the numerical observation. For this narrow beam, this agreement extends as well to the experimental data. On the contrary, for wide enough beams, i.e. above the threshold W_c , in spite of the fact that $\vec{k}_{1,c}$ is almost perpendicular to \vec{k}_0 (a condition enhancing the value of σ_{adv}), the secondary waves have time to grow before leaving the interaction area. Consequently, the central triad becomes dominant when increasing the beam width. In the time evolution of the numerical experiment, this triad appears first, the result derived for infinitely wide beams is thus recovered. At a later time, it is followed by the second triad. Our numerical results confirm that the width of the beam changes the selection of the triad. This new effect explains why energy transfer is mainly towards smaller scales for narrow beams.

5. Oceanic case

This new finite-width theory is therefore of importance when considering internal wave beams from in-situ observations of the ocean (Lien & Gregg 2001; Dewan et al. 1998; Gostiaux et al. 2007). In the ocean, since the wavelengths are larger by several orders of magnitude, the Reynolds number is much larger than in the experiments and

consequently viscous effects can be safely neglected. Consequently, the beam width is the dominating control parameter for the growth rate. We will focus on equatorial regions, for which the background rotation has no effect.

For example, we consider a primary beam with the following typical parameters:

- (a) $\omega_0 = 1.4 \cdot 10^{-4} \text{ rad} \cdot \text{s}^{-1}$, which corresponds to the diurnal M2 tide period.
- (b) $\lambda_0 = 100 \text{ m}$, which corresponds to field measurements in Kaena Ridge, Hawaii (Sun et al. 2013).
- (c) $N = 1.12 \cdot 10^{-3} \text{ rad} \cdot \text{s}^{-1}$. This value of the buoyancy frequency allows a propagation angle of $\theta = 7^\circ$ which is close to oceanic observations.
- (d) the Froude number $Fr = u_0 m_0 / (2\pi N) = 0.035$ (Gayen & Sarkar 2013) which allows us to estimate Ψ_0 .
- (e) the vertical component of the Coriolis force is ignored and the Coriolis parameter f is set to zero.

Figure 5(a) shows the evolution of the growth rate as a function of the width of the beam. With the chosen parameters, the transition between the external and central triad configurations is obtained around $W = 1.5\lambda_0$. Figure 5(b) presents the evolution of the modulus of the secondary wave vectors for the external case (black lines) and the central case (gray lines) as a function of the width of the primary beam. For example for a narrow beam $W = 1\lambda_0$, the maximum of growth rate is obtained on the external branch (5(a)) and PSI enables a transfer to smaller scales: $\kappa_1 = 12\kappa_0$, $\kappa_2 = 11\kappa_0$ (figure 5(b)). This behavior corresponds to simulations (Gerkema et al. 2006; Gayen & Sarkar 2013) and to oceanic observations (McKinnon et al. 2012). Moreover the value of the growth rate predicted by the model ($\sigma = 1.2 \text{ day}^{-1}$) gives a value which has the right order of magnitude when compared to numerical values: 0.5 day^{-1} (Gerkema et al. 2006), or 0.66 day^{-1} (Gayen & Sarkar 2013) and to oceanic measurements: from 0.2 to 0.5 day^{-1} (McKinnon et al. 2012). On the contrary for a larger beam, the instability enables transfer to both larger and smaller scales ($\kappa_1 = 1.7\kappa_0$, $\kappa_2 = 0.7\kappa_0$) which corresponds to the infinitely wide theory prediction.

This transition depends on the amplitude of the stream function Ψ_0 . For example, for Ψ_0 three times larger, the transition is obtained for $W = 0.55\lambda_0$. In contrast, for Ψ_0 three times smaller, the transition is obtained for $W = 4.5\lambda_0$. Thus, the transition between the two behaviors appears for W close to the typical width of an oceanic beam. Consequently, the finite width of the beam can have a notable impact on the selection of the triad in oceanic cases and provides an explanation for the predominance of energy transfer to smaller scales for oceanic narrow beams.

6. Conclusion.

We have shown theoretically, numerically and experimentally that the width of the internal wave beam is a key element in parametric subharmonic instability. This feature had been totally overlooked previously, despite its dramatic consequences on the triad selection mechanism. The subharmonic plane waves that are theoretically unstable can only extract energy from the primary wave if they do not leave the primary beam too quickly. This finite-width mechanism has two opposite consequences on the wave energy dissipation: it introduces a PSI threshold (reducing transfer and therefore dissipation), but when PSI is present it enhances the transfer towards small wavelengths, more affected by dissipation. A complete theoretical study of the impact of the envelope on the PSI will be a timely achievement. We are aware of a recent work about the weakly nonlinear asymptotic analysis of the problem by Karimi & Akylas (2014).

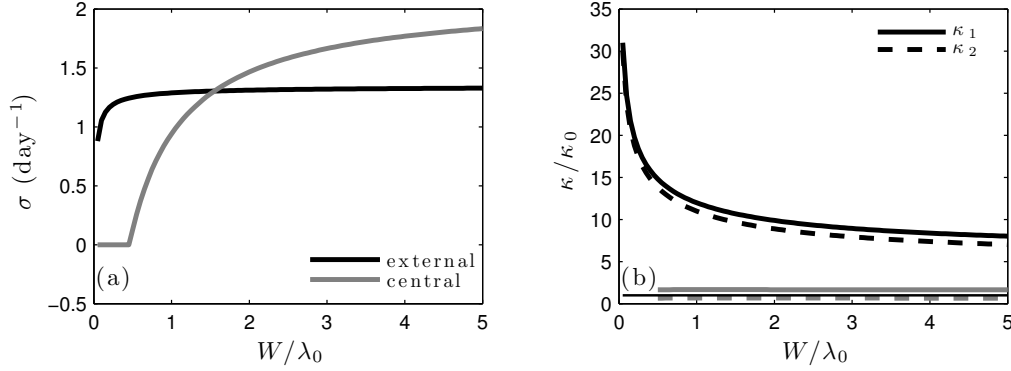


Figure 5: (a) Evolution of the growth rate computed from (3.7) as a function of the width of the beam, computed using the finite-size model in an oceanic case ($N = 1.12 \cdot 10^{-3}$ rad/s, $\omega_0/N = 0.125$, $\lambda_0 = 100$ m, $f = 0$). The transition between the external and central triad configurations is obtained around $W = 1.5\lambda_0$. (b) Evolution of the modulus of the secondary wave vectors for the external case in black and the central case in gray as a function of the width of the beam. The horizontal thin black line represents $\kappa/\kappa_0 = 1$.

It has not escaped our notice that the Coriolis force will significantly modify the prediction. Indeed, the group velocity for inertia-gravity waves, which is proportional to $\sqrt{(\omega^2 - f^2) \cdot (N^2 - \omega^2)} / (\omega\kappa)$, decreases with the Coriolis parameter f (Gill 1982). The rotation reducing the ability of subharmonic waves to escape, it seriously reinforces the instability. At the critical latitude, the group velocity vanishing, one should even recover the theoretical prediction for plane waves.

Finally, from a more fundamental point of view, such a mechanism modifies significantly the transfer of energy between scales and must be taken into account in all analysis (Caillol & Zeitlin 2000; Lvov et al. 2010, 2012) of wave turbulence, in which infinitely wide plane waves are until now the common theoretical objects, but not appropriate for careful predictions.

We thank P. Meunier for insightful discussions. This work has been partially supported by the ONLITUR grant (ANR-2011-BS04-006-01) and achieved thanks to the resources of PSMN from ENS de Lyon. MLB acknowledges financial support from the European Commission, Research Executive Agency, Marie Curie Actions (project FP7-PEOPLE-2011-IOF-298238).

Appendix. Is there an amplitude threshold in resonant triadic instability for an infinitely wide wave beam?

The expression (3.7) shows that, to get a strictly positive growth rate, the amplitude of the stream function has to be larger than

$$|\Psi_s(l_1, m_1)| = \frac{\nu}{2} \sqrt{\frac{\kappa_1^2 \kappa_2^2}{I_1 I_2}}, \quad (6.1)$$

with I_1 and I_2 defined in Eq. (3.6). This expression has already been reported in Koudella & Staquet (2006) and Bourget et al. (2013) with minor typos in the latter case. What has

been overlooked is that the PSI threshold is the global minimum of this function (6.1) of several variables.

In this appendix, we study the behaviour of Ψ_s when \vec{k}_1 tends to \vec{k}_0 , which is the most unstable case for small values of the amplitude. In this case, we assume

$$\ell_1 = \ell_0(1 + \mu_0\epsilon^\alpha), \quad (6.2)$$

$$m_1 = m_0(1 + \epsilon), \quad (6.3)$$

with $\epsilon = o(1)$, $\alpha \geq 1$ and ϵ and μ_0 are positive.

Using the temporal and spatial resonance conditions and the dispersion relation of internal waves, we obtain the relation

$$\frac{m_0^6}{\kappa_0^6} (\epsilon^4 - 2\mu_0\epsilon^{3+\alpha} + o(\epsilon^{2\alpha})) = \mu_0^2\epsilon^{2\alpha}. \quad (6.4)$$

To solve this equation, there are *a priori* two different solutions for α :

(a) $3 + \alpha = 2\alpha$ leading to $\alpha = 3$. However, this value makes it possible to balance terms at order ϵ^6 but not the lower order term ϵ^4 . This value $\alpha = 3$ is therefore not acceptable.

(b) $4 = 2\alpha$ leading to $\alpha = 2$. In that case, the lowest order terms can be balanced and one gets $\mu_0 = (m_0/\kappa_0)^3$.

Finally, we obtain

$$\ell_1 = \ell_0(1 + \mu_0\epsilon^2) \quad \text{and} \quad \ell_2 = -\mu_0\ell_0\epsilon^2 \quad (6.5)$$

$$m_1 = m_0(1 + \epsilon) \quad \text{and} \quad m_2 = -m_0\epsilon. \quad (6.6)$$

With these relations, it can be shown that

$$I_1 = -\ell_0 m_0 \epsilon + o(\epsilon) \quad \text{and} \quad I_2 = -\ell_0 m_0 + o(1), \quad (6.7)$$

which means that

$$|\Psi_s| = \frac{\nu}{2} \frac{N}{\omega_0} \sqrt{\epsilon} + o(\epsilon^{1/2}). \quad (6.8)$$

Therefore, the minimum of the positive expression (6.1) is zero. Consequently, there is no threshold for an infinitely wide wave beam.

REFERENCES

- BENIELLI, D. & SOMMERIA, J. 1998 Excitation and breaking of internal gravity waves by parametric instability. *Journal of Fluid Mechanics* **374**, 117–144.
- BOURGET, B., DAUXOIS, T., JOUBAUD, S. & ODIER, P. 2013 Experimental study of parametric subharmonic instability for internal plane waves. *Journal of Fluid Mechanics* **723**, 1–20.
- CAILLOL, P. & ZEITLIN, V. 2000 Kinetic equations and stationary energy spectra of weakly non-linear internal gravity waves. *Dynamics of Atmospheres and Oceans* **32**(2), 81–112.
- CLARK, H. A. & SUTHERLAND, B. R. 2010 Generation, Propagation and Breaking of an Internal Wave Beam. *Physics of Fluids* **22**, 076601.
- DALZIEL, S. B., HUGHES, G. O. & SUTHERLAND, B. R. 2000 Whole-field density measurements by ‘synthetic schlieren’. *Experiments in Fluids* **28** (4), 322–335.
- DEWAN, E. M., PICARD, R. H., O’NEIL, R. R., GARDINER, H. A., GIBSON, J., MILL, J. D., RICHARDS, E., KENDRA, M. & GALLERY, W. O. 1998 MSX Satellite-observations of thunderstorm-generated gravity-waves in mid-wave infrared images of the upper-stratosphere. *Geophysical Research Letter* **25**, 939–942.
- GAYEN, B. & SARKAR, S., 2013 Degradation of an internal wave beam by parametric subharmonic instability in an upper ocean pycnocline. *Journal of Geophysical Research - Oceans* **118**(9), 4689–4698.

- GERKEMA, T., STAQUET, C. & BOURUET-AUBERTOT, P. 2006 Decay of semi-diurnal internal-tide beams due to subharmonic resonance. *Geophysical Research Letter* **33**, L08604.
- GILL, A. E. 1982 *Atmosphere-Ocean Dynamics*(Vol. 30). Academic Press.
- GOSTIAUX, L., DIDELLE, H., MERCIER, S. & DAUXOIS, T. 2007 A novel internal waves generator. *Experiments in Fluids* **42** (1), 123–130.
- GOSTIAUX, L., & DAUXOIS, T. 2007 Laboratory experiments on the generation of internal tidal beams over steep slopes. *Physics of Fluids* **19**, 028102.
- HINDMARSH, A.C., BROWN, P.N., GRANT, K.E., LEE, S.L., SERBAN, R., SHUMAKER, D.E. & WOODWARD, C.S. 2005 SUNDIALS: Suite of Nonlinear and Differential/Algebraic Equation Solvers. *ACM Transactions on Mathematical Software* **31**, 363–396.
- KARIMI, H.H. & AKYLAS, T. 2014 Parametric subharmonic instability of internal waves: locally confined beams versus monochromatic wavetrains. *Journal of Fluid Mechanics*. (in press)
- KOUELLA, C.R. AND STAQUET, C. 2006 Instability mechanisms of a two-dimensional progressive internal gravity wave *Journal of Fluid Mechanics* **548**, 165–196.
- LIEN, R. C., & GREGG, M. C. 2001 Observations of turbulence in a tidal beam and across a coastal ridge. *Journal of Geophysical Research* **106**, 4575–4591.
- LVOV, Y. V., POLZIN, K. L., TABAK, E. G. & YOKOYAMA, N. 2010 Oceanic Internal-Wave Field: Theory of Scale-Invariant Spectra. *Journal of Physical Oceanography* **40**, 2605–2623.
- LVOV, Y. V., POLZIN, K. L. & YOKOYAMA, N. 2012 Resonant and Near-Resonant Internal Wave Interactions. *Journal of Physical Oceanography* **40**, 669–691.
- MCEWAN, A. D. & PLUMB, R. A. 1977 Off-resonant amplification of finite internal wave packets. *Dynamics of Atmospheres and Oceans* **2** (1), 83–105.
- MCKINNON, J. A., ALFORD, M. H., SUN, O., PINKEL, R., ZHAO, Z. & KLYMAK, J. 2012 Parametric Subharmonic Instability of the Internal Tide at 29°N. *American Meteorological Society* **43** (1), 17–28.
- MERCIER, M. J., GARNIER, N. B. & DAUXOIS, T. 2008 Reflection and diffraction of internal waves analyzed with the Hilbert transform. *Phys. Fluids* **20** (8), 086601.
- MERCIER, M. J., MARTINAND, D., MATHUR, M., GOSTIAUX, L., PEACOCK, T. & DAUXOIS, T. 2010 New wave generation. *Journal of Fluid Mechanics* **657**, 308–334.
- SUN, O. & PINKEL, R. 2013 Subharmonic energy transfer from the semi-diurnal internal tide to near-diurnal motions over Kaena Ridge, Hawai . *Journal of Physical Oceanography* **43**, 766–789.
- SUTHERLAND, B. R. 2013 The wave instability pathway to turbulence. *Journal of Fluid Mechanics* **724**, 1–4.
- SUTHERLAND, B. R., DALZIEL, S. B., HUGHES, G. O. & LINDEN, P. F. 1999 Visualization and measurement of internal waves by ‘synthetic schlieren’. Part I. Vertically oscillating cylinder. *Journal of Fluid Mechanics* **390**, 93–126.
- YOUNG, W. R., TSANG, Y.-K. & BALMFORTH, N. J. 2008 Near-inertial parametric subharmonic instability. *Journal of Fluid Mechanics* **607**, 25–49.